3D Printed Scaffold Based on Polycaprolactone/Self-assembled Fullerene (C_{60}) Nanorod for Bone Tissue Engineering

Novi Dwi Widya Rini [1,2,3], Adel Alshammari [4,5], Candrani Khoirinaya [6], Anggraini Barlian [6,7], Lia Amelia Tresna Wulan Asri [3], Glen Cooper [4], Katsuhiko Ariga [1,8], Lok Kumar Shrestha [1,2,*] and Arie Wibowo [3,7,*]

[1] Research Center for Materials Nanoarchitectonics (MANA), National Institute for Materials Science (NIMS), 1-1 Namiki, Tsukuba, Ibaraki 305-0044, Japan

[2] Department of Materials Science, Institute of Pure and Applied Sciences, University of Tsukuba, 1-1-1 Tennodai, Tsukuba, Ibaraki 305-8573 Japan

[3] Materials Science and Engineering Research Group, Faculty of Mechanical and Aerospace Engineering, Institut Teknologi Bandung, Jl. Ganesha 10, Bandung, 40132, Indonesia

[4] Department of Mechanical, Aerospace, and Civil Engineering, University of Manchester, Manchester M13 9PL, UK

[5] Engineering College, University of Hail, Hail 55476, Saudi Arabia

[6] School of Life Sciences and Technology, Institut Teknologi Bandung, Jl. Ganesha 10, Bandung 40132, West Java, Indonesia

[7] Research Center for Nanoscience and Nanotechnology, Institut Teknologi Bandung, Jl. Ganesha 10, Bandung 40132, West Java, Indonesia

[8] Department of Advanced Materials Science, Graduate School of Frontier Sciences, The University of Tokyo, 5-1-5 Kashiwanoha, Kashiwa 277-8561, Chiba, Japan

[*]Corresponding author: shrestha.lokkumar@nims.go.jp (L.K.S) and ariewibowo@itb.ac.id (A.W)

Abstract

3D printed polycaprolactone (PCL)-based scaffolds have garnered attention in bone tissue engineering due to their biocompatibility, biodegradability, and precise geometry control. However, it is yet challenging to tune the mechanical properties and hydrophilicity. This paper reports a subtle balance between the mechanical properties and hydrophilicity of the scaffold essential in bone tissue engineering using self-assembled fullerene (C_{60}) nanorods (FNR) and Pluronic 123 surface-modified fullerene nanorods (PFNR) as the reinforced filler. FNR incorporated (0.013 wt%) PCL scaffold (PCL_FNR_0.013) shows enhanced compressive strength (8.4 MPa) and Young's modulus (146.2 MPa), compared to the PCL scaffold (compressive strength: 3.3 MPa and Young's modulus: 56.2 MPa) without significant changes in the hydrophilicity. However, the PCL scaffolds' hydrophilicity and mechanical properties could be improved by incorporating PFNR filler. As a result, the scaffold shows excellent proliferation activity of Human Wharton's Jelly Mesenchymal Stem Cells. Moreover, both the FNR and PFNR-incorporated PCL scaffolds show antibacterial properties essential to prevent implant-associated infections. The antibacterial activity results reveal that FNR without surface modification offers better antibacterial activity than PFNR, particularly against *Staphylococcus aureus* and *Escherichia coli*. This study demonstrates that by adjusting the type and concentration of fillers, one can tune the mechanical and wetting properties of the PCL scaffold to optimize cell proliferation and antibacterial activity for potential applications in bone tissue engineering.

Keywords: 3D printing, bone tissue engineering, fullerene nanorod, hydrophilicity, polycaprolactone.

1. Introduction

Bone grafts are the second most common medical case worldwide after blood transfusions [1]. Like with other body parts, bones can regenerate and reconstruct by themselves. Many factors influence the healing process, including the size of the damage gap and the amount of bone loss [2,3]. Increased bone loss could limit natural healing and reconstruction, resulting in failure, various complications, and, in the worst case, death [4,5]. Bone grafts bridge the gap and replace the bone loss to facilitate regeneration and reconstruction [6,7]. However, autograft and allograft, the gold standard, have drawbacks due to the limited supply [8,9]. Another potential approach is the fabrication of synthetic scaffolds because their properties can be tuned so that the scaffold acts as passive support and stimulates the growth and regeneration of the bone [10,11].

To successfully apply scaffolds in bone tissue engineering, the scaffold must mimic the extracellular matrix of bone tissue to facilitate cell attachment and tissue formation. Furthermore, the scaffold's porosity must be interconnected to allow molecules and nutrients to penetrate the interior of the scaffold and support continuous tissue growth [12,13]. The method extensively explored to produce scaffolds with the required porous materials is three-dimensional (3D) printing fabrication, also known as additive manufacturing [14,15]. 3D printing can construct complex geometries with high control parameters, such as pore size, shape, porosity, and pore interconnection. However, challenges still exist with material selection and 3D shape specificity due to the specific properties of each material, such as the melting point and degradation temperature, which will affect the processing parameters and the final construction [16,17].

Polycaprolactone (PCL) fabricated using the 3D printing method has been shown to have an excellent porous structure [18]. PCL is particularly well-suited for 3D printing compared to

other polymers due to its low melting point of 58 – 60 °C. This melting point allows for easy processing, tailored extrusion, and rapid cooling, resulting in rigid and highly precise scaffolds [19]. Moreover, PCL degrades more slowly compared to other polymer-based implants, taking up to four years, which makes PCL an attractive choice for long-term implants [20,21]. However, the high hydrophobicity causes cell attachment to the scaffold less than optimal [22]. In addition, PCL needs to be blended with other materials to get the required mechanical strength due to its low mechanical properties [23]. Therefore, selecting suitable filler material is essential to improve the overall characteristics of the scaffold [24].

Recently, carbon-based nanomaterials such as fullerenes (C_{60}) [25], graphene [26,27], and carbon nanotubes [26], have been extensively employed as the polymer composites' reinforcement filler. Considering that fullerene (C_{60}) has theoretically Young's modulus of 1980 GPa for its single molecule [28], it could be expected that the addition of a few fullerenes could significantly increase the mechanical strength of the polymer. It has been found that the incorporation of a small amount of fullerenes (C_{60} or C_{70}: 0.02 to 0.08 wt%) in thermoplast-based polymer nanocomposite increases Young's modulus and tensile strength of the nanocomposites by 30-40%[29]. Rajagopalan and coworkers also showed that adding 0.1 wt% of fullerene (C_{60}) drastically increases Young's modulus of the nanocomposite membrane [30]. Moreover, previous investigation has shown that the addition of a small amount of C_{60} nanoparticles in a hydroxyapatite-chitosan composite shows an antibacterial effect [31], which is crucial in bone tissue engineering due to the bacterial infections that often occur after bone surgery [32,33]. These infections can lead to morbidity or even fatalities in severe cases, such as septic arthritis [34] and peri-implantitis [35]. PCL does not show any antibacterial effect; therefore, it is promising to use C_{60} as a reinforcement filler and antibacterial agent in the PCL matrix [36].

Nevertheless, the use of zero-dimensional (0D) C_{60} in a composite is not favorable due to its tendency to form uncontrollable aggregates. Meanwhile, self-assembled C_{60}-based nanomaterials with higher dimensions, such as C_{60} nanorods, have a lower tendency to form aggregates, thus, more favorable for composites [37]. Even though C_{60} nanorods have various potential applications, their application in biomedical field is still limited due to hydrophobic nature of C_{60} [30]. Therefore, a surface modification is required to hydrophilize its surface and to promote the scaffold and cell interactions [38]. Wong et al. showed that the self-assembled C_{60} nanorod coated with Pluronic 123 (P123) exhibits hydrophilic properties compared to the nanorods before the P123 coating [39]. P123 is known as a triblock copolymer consisting of polyethylene oxide (PEO) as a hydrophilic segment and polypropylene oxide (PPO) as a hydrophobic segment [40]. The hydrophobic C_{60} is encapsulated within the PPO core, while the hydrophilic PEO segments form the outer shell, resulting in the hydrophilic surface of C_{60}[41]. To our knowledge, surface-modified self-assembled C_{60} nanorods have not been explored as a filler material in a 3D PCL scaffold.

In this contribution, we report the fabrication of porous scaffolds composed of PCL and P123 surface-modified C_{60} nanorods using 3D printing. The filler materials were self-assembled fullerene C_{60} nanorods (FNR) and P123 surface-modified fullerene nanorods (PFNR). FNR was prepared using the liquid-liquid interfacial precipitation (LLIP) method [42], and its surface was modified with the different concentrations of P123. The mechanical properties, hydrophilicity, cell viability, cell proliferation, and antibacterial activities of the 3D-printed PCL-FNR or PCL_PFNR scaffolds were then evaluated. In this study, human Wharton's jelly mesenchymal stem cells (hWJ-MSCs) were chosen as precursor cells for cell viability and cell proliferation of the prepared scaffold because hWJ-MSCs offer several advantages, including source availability, providing

high cell yield with non-invasive method, demonstrating excellent proliferation, and exhibiting a fibroblast-like morphology [43,44]. Furthermore, our prior work demonstrated that by day 21 of treatment, hWJ-MSCs had differentiated into mature osteoblasts on a PCL-based 3D scaffold [44]. Another study also indicated that hWJ-MSCs are suitable for evaluating initial cellular responses to materials in bone tissue engineering applications [45]. Based on our evaluation, we have found that the addition of FNR enhances the mechanical properties, while the addition of PFNR enhances the hydrophilicity and cell proliferation of the scaffolds. In addition, all the scaffolds with the addition of FNR and PFNR filler show antibacterial activity against *E. coli* and *S. aureus*.

2. Materials and Methods

2.1. Materials

Pristine fullerene C_{60} was purchased from MTR Ltd, USA (purity 99.5%). Mesitylene (99.8%), methanol (99.7%), and isopropyl alcohol (99.7%) were purchased from Wako Chemicals Corporation, Tokyo, Japan and were used as received. Polycaprolactone pellets (CAPA 6500, MW = 50,000 g/mol, melting point = 58 – 60 °C, density = 1.146 g/mL) provided by Perstorp (Warrington, UK) were used as received to prepare composite blends with self-assembled C_{60} nanorods. Poly(ethylene glycol)-*block*-poly(propylene glycol)-*block*-poly(ethylene glycol: Pluronic 123) was purchased from Sigma-Aldrich, USA. *Staphylococcus aureus* (*S. aureus*; ATCC 3658) and *Escherichia coli* (*E. coli*; ATCC 8939) bacterial strains were obtained from the Microbiology Laboratory, School of Pharmacy, Institut Teknologi Bandung (ITB).

2.2. Preparation and characterization of hydrophilic self-assembled fullerene nanorod

Fullerene C_{60} solution (1 mg/mL) was prepared in mesitylene by dissolving a required amount of pristine C_{60}, and fullerene C_{60} nanorod (FNR) was synthesized using the static liquid-liquid interfacial precipitation (LLIP) method [37]. In a typical synthesis, C_{60}/mesitylene solution (1 mL) was taken in a 13.5 mL glass vial, and anti-solvent methanol (3 mL) was then added slowly on top and the system was left undisturbed for 30 min avoiding mechanical disturbance. The system was then sonicated for 1 min and incubated for 24 hours at 25 °C. The following 24 hours later, the FNRs were isolated by repeated centrifugation and washed with isopropyl alcohol (IPA) three times. Finally, the precipitate was dried in a vacuum oven for 24 hours.

The surface of FNR was coated with Pluronic 123 by adding FNR powder to a solution containing 0.5 wt% Pluronic 123 in DI water [39]. After 24 hours of resuspension, the supernatant was removed by centrifugation, and the precipitate was dried for 24 hours by freeze-drying.

The morphology of FNR and PFNR were observed by scanning electron microscope (SEM, Hitachi model S-4800, Japan). Fourier-Transform Infrared (FTIR) was carried out using attenuated total reflection (NICOLET iS20). Raman spectra were acquired using an NRS-3100 Raman spectrometer. The charge on the surface of FNR and PFNR was measured utilizing a Horiba SZ-100 Nano Particle Analyzer.

2.3. Fabrication of PCL/FNR and PCL/PFNR 3D-printed scaffold

A composite premix was prepared using the melt blending approach [46]. The variants of the composite premix developed in this study are as follows: pure PCL (without fillers); PCL_FNR_0.013 (PCL with 0.013 wt% FNR); PCL_PFNR_0.0013 (PCL with 0.0013 wt% PFNR); PCL_PFNR_0.013 (PCL with 0.013 wt% PFNR); and PCL_PFNR_0.13 (PCL with 0.13 wt% PFNR). Each composite premix was subsequently fabricated utilizing screw-assisted

extrusion-based 3D printing equipment (3D Discovery, regenHU, Villaz-St-Pierre, Switzerland). During the 3D printing process, the composite premix was placed into a reservoir and melted at 90 °C. After the premix had melted homogeneously in the reservoir, it was pumped into the screw chamber via air pressure in the tool. Next, the premix was extruded using a 500 µm needle. The premix that exited the extruder was liquid and created filaments with layer orientations ranging from 0 to 90 degrees. The extrusion process adjusted the deposition speed and screw rotation speed parameters. Finally, the scaffold was cooled layer by layer, resulting in a solid 3D scaffold.

2.4. Characterization of PCL/FNR and PCL/PFNR 3D-printed scaffold

For the 3D scaffold, the morphology was characterized by SEM, Hitachi model SU-3500 at an accelerating voltage of 10 kV. Scaffold porosity represents the percentage of measured scaffold density (scaffold mass divided by apparent volume, neglecting the pores) and the initial density of material (measured using the psychometry method, considering the pores) [47]. The compressive strength of the scaffold was measured using a Universal Testing Machine, Tensilon RTF-1310, A&D Company. The sessile drop method (Contact Angle Meters, Kyowa) was used to measure the contact angle by dropping 2 µL of water on the surface of the scaffold. The droplet was recorded 1 second after dropping. All measurements were carried out with a 5 mm x 5 mm x 3 mm (triplicate) scaffold.

Cell viability and cell proliferation on the scaffold were determined using the colorimetric method (3-(4,5-dimethylthiazol-2-yl)-2,5-diphenyltetrazolium bromide (MTT assay) [48,49]. Before the MTT test, Human Wharton's Jelly Mesenchymal Stem Cell (hWJ-MSC) cells were cultured on scaffolds at a concentration of 1 x 10^5 cells/well in microplates with a flat bottom using Dulbecco's Modified Eagle media (DMEM). Cell culture incubation was carried out at 37 °C, with

CO_2 levels ranging from 5-6.5% in the cell culture incubator. The MTT test was performed on each 3 days of incubation. To perform the MTT test, 10 µL of reagent was added to each well. The cells were then incubated for another 4 hours in a cell culture incubator. Next, 100 µL of PBS was applied to each well. The absorbance of the dissolved purple formazan crystals was then measured using an ELISA reader, Bio-Rad iMark, at a wavelength of 595 nm.

The scaffolds' antibacterial properties were determined by the total plate count (TPC) [50]. The bacterial suspension (*E. coli* and *S. aureus*) was prepared by adding one culture cycle of bacteria to Mueller Hinton Broth (MHB) media and incubated at 37 °C for 24 hours. After that, the turbidity of the bacteria suspension was measured to be equivalent to 0.5 Mc Farland. The suspension was diluted 1:20 with MHB medium. The test bacteria were then decimally diluted by pipetting 1 mL into the first vial containing 9 mL of 0.9% NaCl with a 10^{-6} dilution. Then, 1 mL of the 10^{-6} dilution was placed in a sterile petri dish, and 20 mL of Mueller Hinton Agar (MHA) was added to the petri dish. The diffusion method was obtained by putting the sample on MHA media and pouring another Agar covering the sample. The incubation was done for 24 hours at 37 °C. Using a caliper, the diameter of the encountered obstruction was determined. Next, 100 µL of top agar from the inhibition region was mixed with 900 µL of 0.9% NaCl solution (dilution 10^{-1}). The dilution was increased to decimal 10^{-8}. The TPC was then performed in triplicate and incubated for another 24 hours at 37 °C. Following that, the number of colonies that grew was counted.

2.5. Statistical analysis

Each experiment was tested with a minimum of three replicates. Statistical analysis was conducted with Origin 9 (Originlab, USA) and Prism 10 (GraphPadm USA), and its statistical

significance was ascertained when $P < 0.05$. One-way ANOVA was used to make statistical comparisons for studies with more than 2 groups, while hWJ-MSC's cell viability was assessed using Two-way ANOVA repeated measures. Post-hoc analysis was performed via Tukey's multiple comparison test. All values are expressed as mean ± standard deviation (SD) or mean ± standard error of the mean.

3. Results and Discussion

3.1. Preparation and characterization of hydrophilic self-assembled fullerene nanorod

Self-assembled fullerene nanorods (FNRs) with a uniform size distribution were prepared using the static LLIP method [51]. The hydrophobic surface of the FNRs was modified with P123 coating to obtain hydrophilic PFNR [39]. The schematic of the preparation of FNR and PFNR is illustrated in Fig. 1.

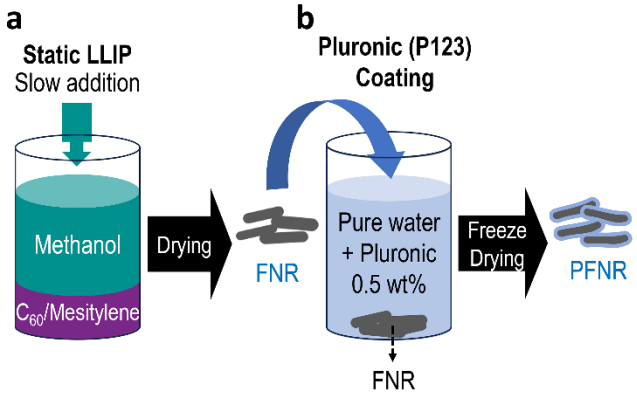

Fig. 1 (a) Scheme of self-assembled fullerene nanorod (FNR) preparation using the static LLIP method and (b) surface-modified hydrophilic self-assembled FNR (PFNR) preparation by coating the FNR with P123.

Owing to the intrinsic hydrophobic properties of fullerene, the FNRs are not dispersible in water (Fig. 2a). On the other hand, after the surface modification, the PFNR could be dispersed in water (Fig. 2b) [42]. SEM observations reveal different surface morphology of the FNR and PFNR. The PFNR (Fig. 2d) has a rougher surface than the FNR (Fig. 2c), confirming successful P123 coating on the FNR surface [39]. It is noting that the SEM images of the PFNR reveal some inhomogeneous surface coating, showing the variations in surface coverage. The histograms of length and diameter distributions of the FNR are shown in Fig. 2e and 2f, respectively. Based on the SEM images, the average length and diameter of FNR are ca. 2,540 ± 751 nm and 160 ± 50 nm, respectively. Due to the rough surface and inhomogeneous surface coatings, we did not plot the histograms of the length and diameter distributions of the PFNRs.

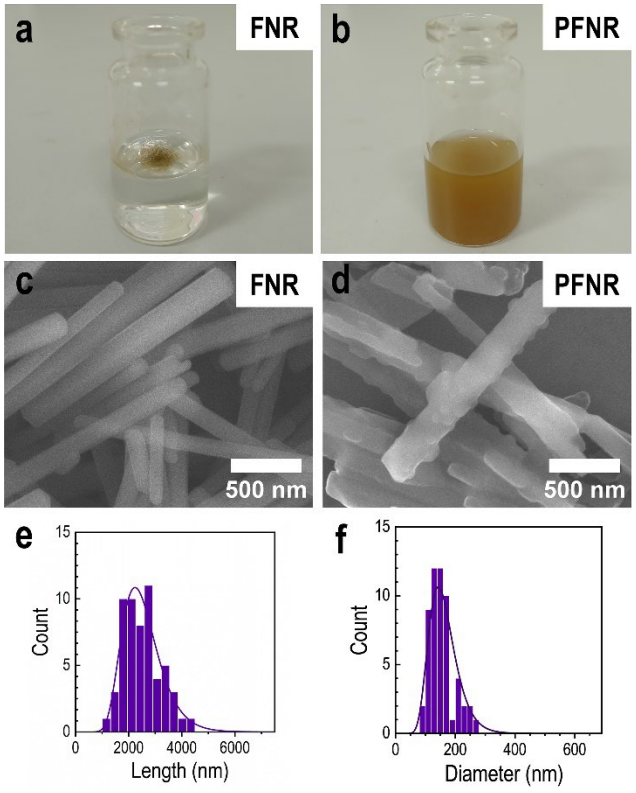

Fig. 2 (a) Digital image showing poor dispersibility of FNR in DI water due to its hydrophobic properties; (b) the corresponding digital image of the PFNR in DI water showing its excellent dispersibility in water due to the surface modification; (c) SEM image of FNR with a smooth surface morphology and (d) PFNR with a rough surface morphology indicating the surface modification by P123 coating; (e) histogram of length and (f) diameter distribution of FNR.

Fig. 3a shows the FTIR spectra of FNR, PFNR, and P123. The FTIR peaks at 575, 1183, and 1428 cm^{-1} present both in FNR and PFNR correspond to the C-C bonds of the C_{60} molecule [30,52]. Aside from this, the new peaks have appeared at 1100 and 2970 cm^{-1}, corresponding to C-O stretching from hydrophilic PEO (1100 cm^{-1}) and antisymmetric CH_3 stretching from hydrophobic PPO (2970 cm^{-1}) [39,53], demonstrating the successful coating of P123 on the FNR surface. The P123 coating was further validated by the surface charge (zeta potential) measurements. The PFNR has a higher negative zeta potential (-57.0 ± 1.6 mV) than the FNR (-3.6 ± 0.3 mV), validating P123 coating [39]. Fig. 3b shows Raman spectra of FNR, PFNR, and pristine C_{60}. All the spectra exhibit prominent peaks corresponding to A_g (1), A_g (2), H_g (1), H_g (2), H_g (3), H_g (4), H_g (7), and H_g (8) bands with no apparent A_g (2) peak shift, indicating that free molecular rotation of fullerene molecules persist both in FNR and PFNR without the polymerization of C_{60} molecules [39].

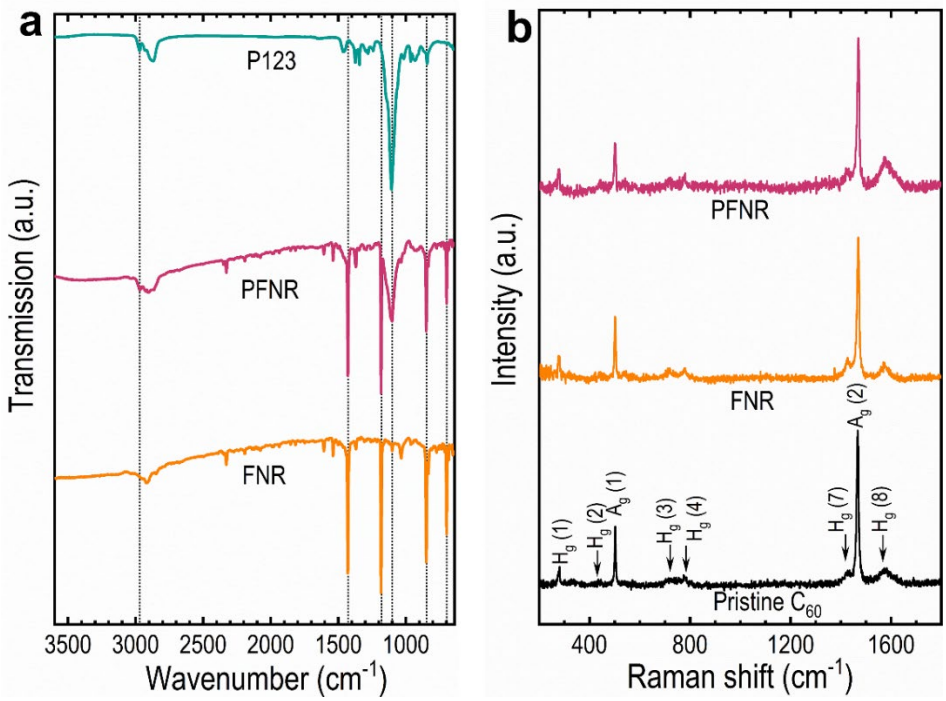

Fig. 3 (a) FTIR spectra of FNR, PFNR, and P123; (b) Raman shift of C_{60} pristine, FNR, and PFNR.

3.2. Fabrication of PCL/FNR and PCL/PFNR 3D-printed scaffold

Fig.4 shows the digital images of the 3D-printed scaffolds (pure PCL, PCL_FNR_0.013, PCL_PFNR_0.0013, PCL_PFNR_0.013, PCL_PFNR_0.13) with dimensions of 25 mm x 25 mm x 3 mm. The scaffold with pure PCL is white, the same as the PCL pellet color. However, FNR and PFNR-incorporated scaffolds have different colors, and the color depends on the concentration. As can be seen in Fig. 4, the PCL_FNR_0.013 scaffold has a yellowish-brown color. Due to very low concentration, the color of the PCL_PFNR_0.0013 scaffold (Fig. 4c) is similar to the pure PCL scaffold (Fig. 4a). The color became intense and brownish at higher concentrations of PFNR in the PCL_PFNR_0.13 scaffold (Fig. 4e).

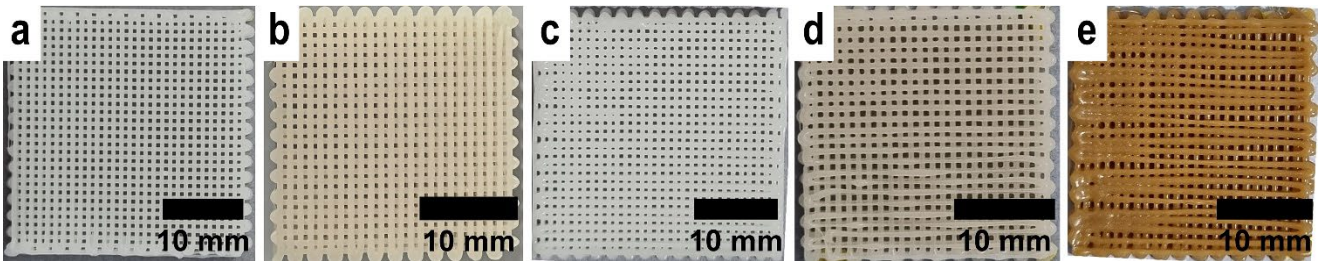

Fig. 4 Top view optical images of the 3D-printed scaffold (a) pure PCL; (b) PCL_FNR_0.013; (c) PCL_PFNR_0.0013; (d) PCL_PFNR_0.013; and (e) PCL_PFNR_0.13.

3.3. Characterization of PCL/FNR and PCL/PFNR 3D-printed scaffold

3.3.1. Scaffold Morphology

The scaffold's surface morphology, filament size, pore size, and porosity were studied by SEM analyses. The illustration of the top view and cross-section view of the scaffold during SEM observation is provided in Fig. 5a and SEM images of the top view and cross-sectional view of the scaffolds are presented in Fig. 5b and Fig. 5c respectively. As can be seen in SEM images from the top view of the scaffolds that were taken at low magnification (Fig. 5b), all the scaffolds were well-aligned with relatively uniform in their shapes, filaments and pores size. SEM images from the top view (Fig. 5b) and cross section (Fig. 5c) of the scaffolds that were taken at medium magnification showed that all the scaffolds have rough surfaces regardless the filler and its concentration. The rough surface could be attributed to the rheological characteristics of the material, which influence the extrusion flow in the 3D printing process [54].

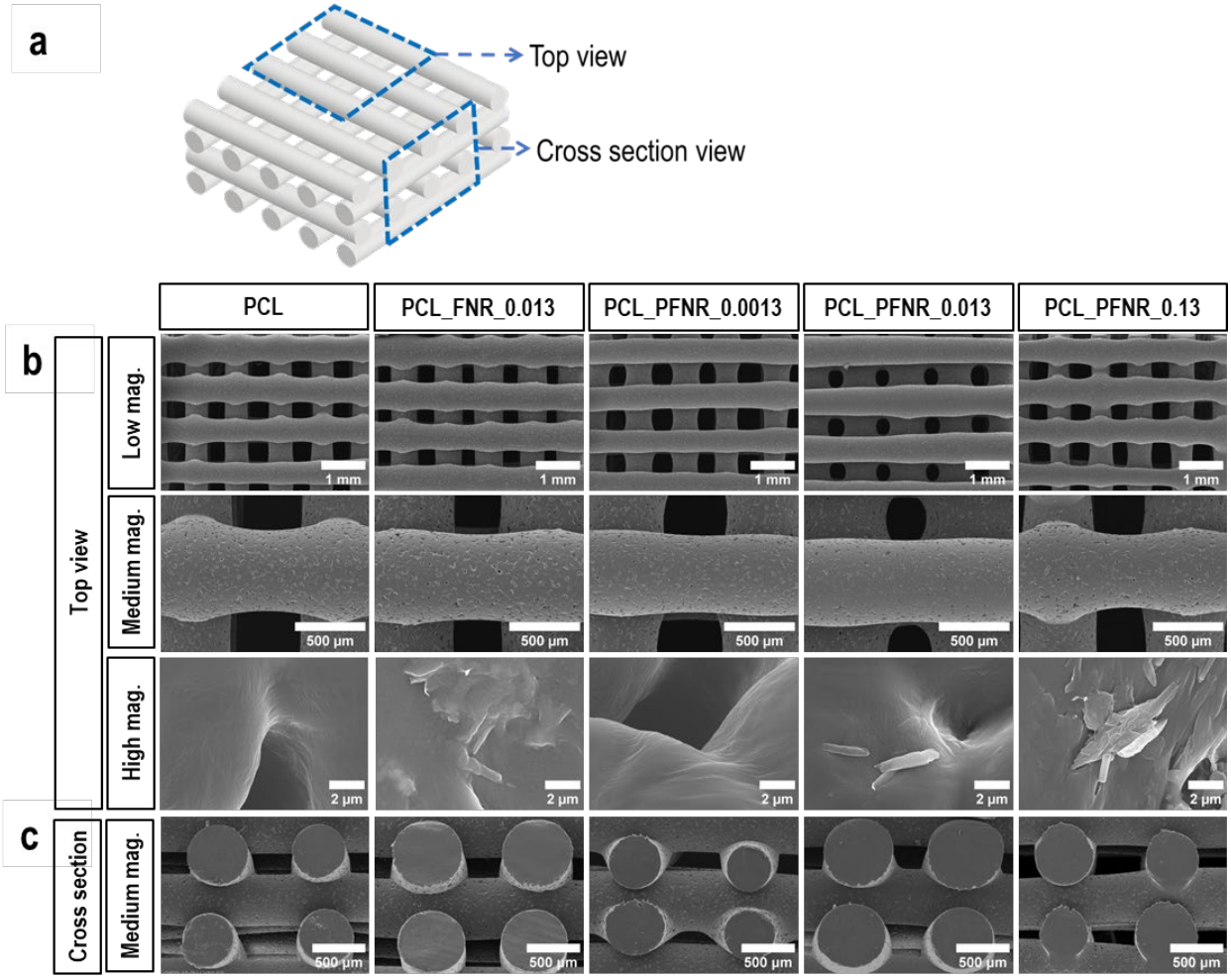

Fig. 5 (a) The illustration of the top view and cross-section view of the scaffold; the SEM images of the scaffold from (b) the top view and (c) the cross-section view.

The filament diameter and pore size and porosity of the scaffolds are summarized in Table 1. The pore diameters of all the scaffolds are higher than 300 μm, which are suitable for promoting angiogenesis and osteogenesis, enhancing the production of new bone in bone tissue engineering applications [55].

Table 1. The filament diameter, pore size, and porosity of each scaffold.

Scaffold	Filament diameter (μm)	Pore size (μm)	Porosity (%)

PCL	506.8 ± 30.7	422.2 ± 28.7	54.6 ± 6.5
PCL_FNR_0.013	613.1 ± 28.6	407.6 ± 26.3	47.7 ± 3.1
PCL_PFNR_0.0013	536.1 ± 39.7	481.4 ± 26.8	53.5 ± 3.2
PCL_PFNR_0.013	617.6 ± 48.1	448.6 ± 21.8	56.7 ± 5.2
PCL_PFNR_0.13	537.6 ± 40.3	450.9 ± 48.7	57.4 ± 5.0

277 *3.3.2 Mechanical Properties*

278 The scaffold is supposed to endure compressive loads, including the body weight and
279 external load when implanted in patients [13]. Young's modulus of healthy human cancellous bone
280 has been reported to range from 100 to 5000 MPa, and the compressive strength ranges from 1 to
281 12 MPa [56]. Fig. 6 shows the representative compressive stress-strain curves of the 3D-printed
282 scaffolds. In this study, Young's modulus was determined as the gradient in the linear elastic
283 region, and the compressive strength was specified as a stress in 10% strain (ISO 844-2014).

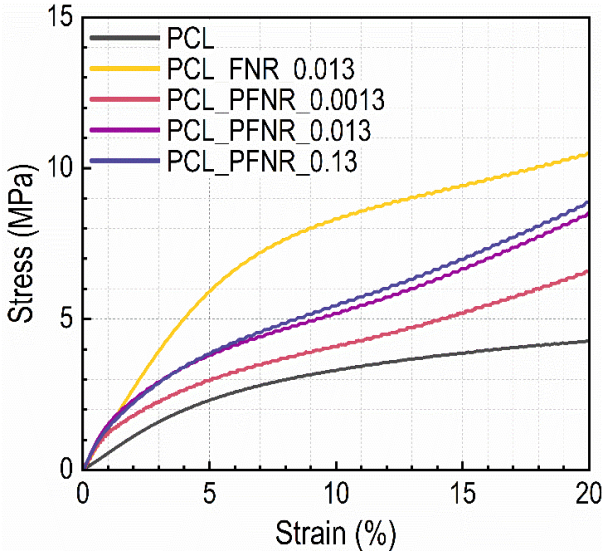

284

285 **Fig. 6** Representative compressive stress-strain curves of 3D-printed scaffolds.

286 Table 2 summarizes the mechanical properties of 3D-printed scaffolds. The pure PCL
287 scaffold has the lowest Young's modulus (56.2 ± 4.2 MPa), which increased drastically (260%:

146.2 ± 5.5 MPa) upon the addition of 0.013 wt% FNR. Young's modulus increases by over 200% in the PFNR system. Our previous report showed that a PCL-based 3D scaffold with 2 wt% polyaniline (PANI) increased the compressive Young's modulus only up to 120% (82.61 ± 6.94 MPa) [15]. Another study using 3 wt% multi-walled carbon nanotube (MWCNT) filler showed 170% (88 ± 3 MPa) increase in Young's modulus [57]. These results highlight that FNR and PFNR provide superior reinforcement compared to PANI and MWCNT. Moreover, Young's modulus of scaffolds with the addition of FNR and PFNR filler is within the range of healthy human cancellous bone [56]. This alignment is crucial since a mismatch of Young's modulus can result in stress shielding and failed bone regeneration [58].

Table 2. The compressive Young's modulus and compressive strength of 3D-printed scaffolds.

Scaffold	Compressive Young's Modulus (MPa)	Compressive Strength (MPa)
PCL	56.2 ± 4.2	3.3 ± 0.1
PCL_FNR_0.013	146.2 ± 5.5	8.4 ± 0.1
PCL_PFNR_0.0013	119.9 ± 5.7	3.7 ± 0.4
PCL_PFNR_0.013	128.0 ± 5.2	4.7 ± 0.5
PCL_PFNR_0.13	138.4 ± 2.5	5.3 ± 0.4

PCL with FNR filler has a higher modulus value than PCL with PFNR filler (Table 2) due to the strong hydrophobic interfacial interaction between the PCL matrix and FNR, which inhibits the movement of polymer chains during compression [59]. Meanwhile, hydrophilic PFNR has no specific interfacial interaction with hydrophobic PCL. As a result, PFNR in the PCL matrix is less rigid and has a lower inhibitory effect on polymer chain movement during compression.

The compressive strength follows the same trend as Young's modulus results (Table 2). Based on the compressive stress-strain curves (Fig. 6), the scaffolds have reached the plastic area at 10% strain. Due to the presence of hydrophobic interfacial interaction between PCL and FNR, more significant load is required to compress the scaffold, resulting in a higher compressive strength [59]. On the other hand, due to the lack of specific interactions between PCL and PFNR, compression occurs independently, which lowers the required compressive load, and hence, low compressive strength is observed in the PFNR system. These results highlight that surface modification leads to different reinforcement results.

3.3.3 Hydrophilicity

The hydrophilic surface is preferable for cell attachment compared to the hydrophobic surface [60]. We tried to tune the hydrophilicity of the PCL_FNR scaffold by modifying the FNR's surface with P123 coating. Fig. 7 shows the contact angles of the prepared scaffolds. Since the measurements were taken immediately (1 second) after water dropping on the scaffold's surface, the surface properties played a more significant role in determining the contact angle than the porosity, as there was no time for the water to penetrate the pores.

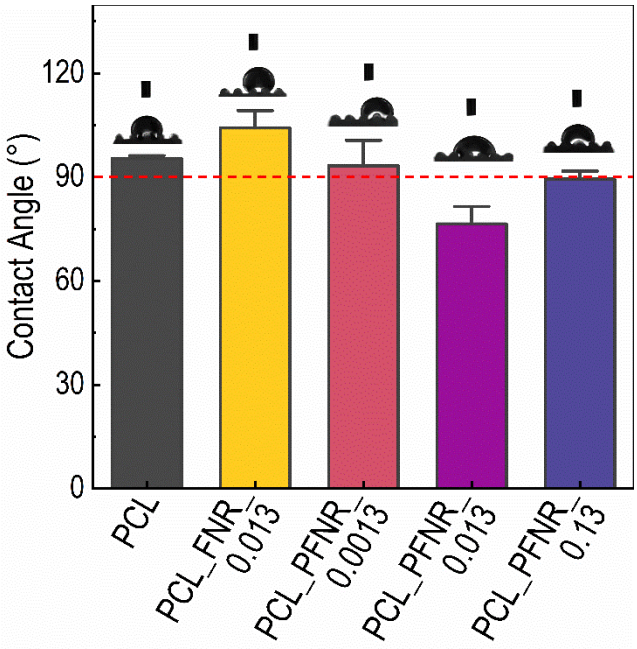

Fig. 7 Contact angles of PCL and FNR and PFNR added PCL scaffolds along with the water droplet images (1 second) on each 3D-printed scaffold. The red horizontal dash line at 90° indicates the threshold to distinguish between hydrophilic and hydrophobic. The values of the contact angle are as follows: PCL (95.4° ± 0.8°), PCL_FNR_0.013 (104.2° ± 7.8°), PCL_PFNR_0.0013 (93.3° ± 6.6°), PCL_PFNR_0.013 (76.5° ± 4.4°), PCL_PFNR_0.13 (89.4° ± 3.2°).

Fig. 7 shows that adding 0.013 wt% FNR to the PCL scaffold increases the contact angle, making the scaffold more hydrophobic. This is because of the intrinsic hydrophobic properties of PCL and FNR [55,61]. The hydrophobic nature likely strengthens the non-polar interactions between the scaffold and water, resulting in higher contact angle values [62]. In contrast, the addition of 0.0013 wt% and 0.013 wt% PFNR considerably reduces the contact angle, giving the scaffold hydrophilic properties. SEM images that were taken at high magnification from the top view of the scaffolds with FNR 0.013 wt% and PFNR 0.013 wt% (Fig. 5b) revealed that the presence of P123 as surface modifier in PFNR could reduce aggregation of the filler in the

fabricated scaffold. P123 likely introduced hydrophilic functional groups to the surface of the filler, promoting better interaction with water molecules and thus lowering the contact angle [63]. However, when the PFNR concentration is increased further to 0.13 wt%, the contact angle unexpectedly increases. This unexpected increase in contact angle may be attributed to several factors. The aggregation of PFNR particles might occur in higher concentrations, reducing their effective surface area for hydrophilic effect [64]. As shown in SEM images that were taken at high magnification from the top view of the scaffolds with PFNR as filler, aggregation became more pronounced as the concentration of PFNR in scaffold increased from 0.0013 wt% to 0.13 wt% (Fig. 5b). This phenomenon likely occurs because PFNR particles tend to cluster together at higher concentrations, limiting their dispersion and reducing their effective surface area in the fabricated scaffolds, which in turn affects hydrophilicity. Another possible reason is that 0.13 wt% might be a saturation point where PFNR does not further enhance hydrophilicity and instead leads to a more heterogeneous surface, causing inconsistent interactions with water [65]. These results indicate that the balance concentration, 0.013 wt% PFNR, is optimal for achieving the best hydrophilic scaffold.

3.3.4 Cell Viability

The viability of human Wharton's Jelly Mesenchymal Stem Cell (hWJ-MSC) on each scaffold was determined using the MTT assay after 72 hours of cell incubation. Fig. 8 depicts a graph of cell viability percentages. Notably, the PCL_PFNR_0.013 demonstrated the highest cell viability (90.4 ± 4.3%), surpassing the viability observed with pure PCL (84.9 ± 9.7%). This suggests that PFNR enhances the scaffold's surface properties at this concentration, promoting better cell adhesion. Conversely, both PCL_PFNR_0.0013 and PCL_PFNR_0.13 resulted in decreased cell viability. However, the cell viability of all scaffolds is above 70%, which meets the

standards of ISO 10993-5:2009 for in vitro cytotoxicity. This signifies that the scaffolds prepared in this study do not exhibit substantial toxicity towards hWJ-MSC.

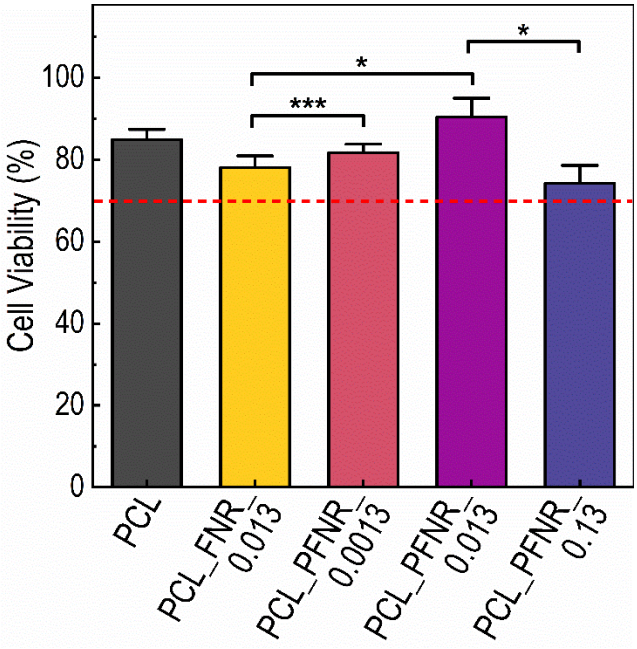

Fig. 8 Cell viability diagram of hWJ-MSCs after 72 hours grown on various 3D-printed scaffolds was assessed by MTT (n=5). *Denotes a significant difference in cell viability ($P < 0.05$). ***denotes a significant difference in cell viability ($P < 0.001$). The values of the cell viability are as follows: PCL (84.9 ± 9.7 %), PCL_FNR_0.013 (78.1 ± 2.5 %), PCL_PFNR_0.0013 (81.7 ± 1.9 %), PCL_PFNR_0.013 (90.4 ± 4.3 %), PCL_PFNR_0.13 (74.3 ± 4.2 %).

3.3.5 Cell Proliferation

The proliferation of hWJ-MSC cells on each scaffold was assessed using the MTT assay (absorbance at 595 nm) up to 12 days of incubation. Fig. 9 shows an increase in cell proliferation for all scaffolds from day 3 to day 12 of incubation.

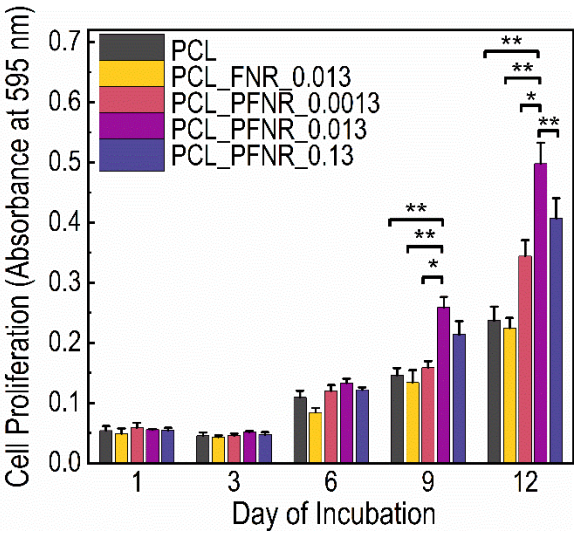

Fig. 9 Graph of hWJ-MSC cell proliferation from day 1 to day 12 on each 3D-printed scaffold which was assessed by MTT (n=3). *denotes a significant difference in cell viability ($p < 0.05$). **denotes a significant difference in cell viability ($p < 0.01$).

Notably, the PCL scaffold with a filler of PFNR has a higher cell proliferation than the pure PCL scaffold and PCL scaffold with a hydrophobic FNR. Among the PFNR-filled scaffolds, the PCL_PFNR_0.013 showed the highest cell proliferation, followed by PCL_PFNR_0.13 and PCL_PFNR_0.0013. These results indicate that the presence of hydrophilic PFNR, particularly at the optimal concentration of 0.013 wt%, enhances the scaffold's capacity to support cell growth more effectively than pure PCL or FNR-filled scaffolds. This trend is consistent with the contact angle results, suggesting that the lower contact angle leads to better cell attachment [44]. A hydrophilic surface increases the binding of the adhesive molecules on the substrate, making the substrate favorable for cell growth and proliferation [38]. Consequently, the scaffold with 0.013 wt% PFNR, which has the lowest contact angle, provided the most hydrophilic surface, leading to the highest cell proliferation.

3.3.6 Antibacterial Activity

Since PCL does not show any antibacterial effect, we added FNR and PFNR to provide antibacterial activity in the scaffold [36,66]. Previous studies indicated that the addition of fullerene in chitosan nano-conjugate enhances its antibacterial action specifically against *S. aureus*, a major pathogen causing infections in the bones and joints [67]. Moreover, incorporating fullerene into a phosphate-alginate composite unaffected by the normobiota (beneficial bacteria in the oral cavity), suggests that this material can be safely used in medical applications [68].

We evaluated the antibacterial properties of the scaffolds against Gram-positive *E. coli* (ATCC 8939) and Gram-negative *S. aureus* (ATCC 6538). As shown in Fig. 10a and 10b, all scaffolds with the addition of FNR and PFNR show antibacterial activity against *E. coli* and *S. aureus*. Compared to the control, all scaffolds significantly decreased (more than 99%) the number of bacteria colonies. This is consistent with the previous study that demonstrated the addition of a small amount of aggregated fullerene (0.00004 wt% nano-C_{60}) to the culture medium, resulting in antibacterial activity against *E. coli* [69]. A previous study showed that Gram-positive bacteria tend to be more susceptible than Gram-negative due to the interaction between fullerene molecules and bacterial cell walls. Fullerenes reduces the proportion of unsaturated fatty acids and increases the proportion of cyclopropane fatty acids in the bacterial cell wall [70]. However, this study shows that the reduction of Gram-positive and Gram-negative has a similar percentage. It might be caused by unspecific filler interactions with membrane proteins and other vital molecules due to the different forms of fullerene [71].

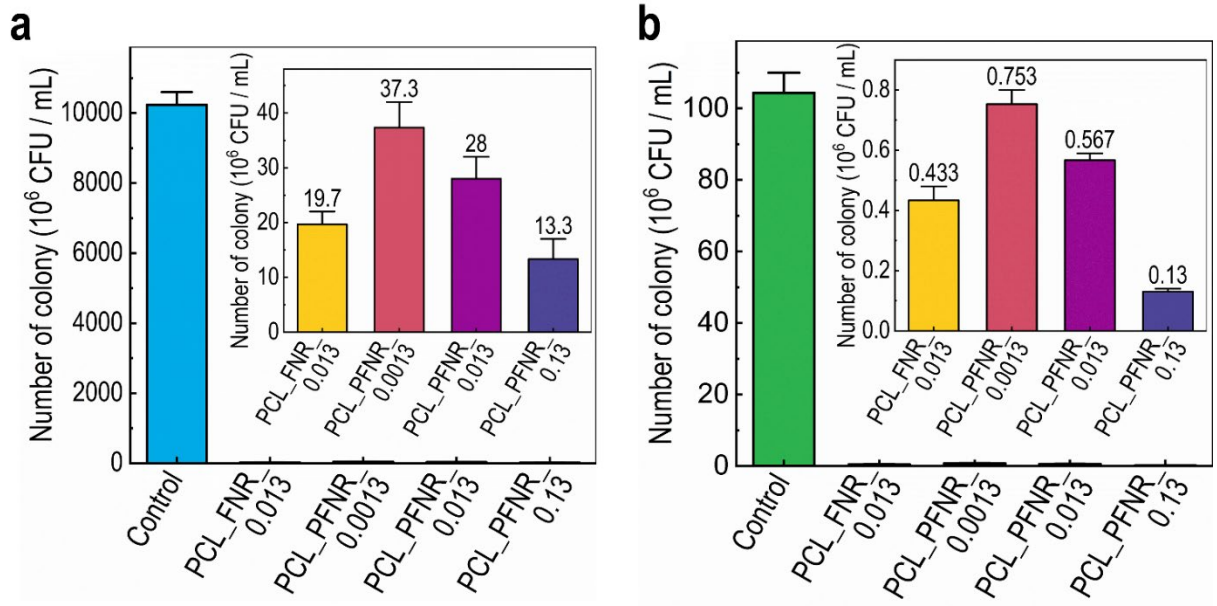

403

404 **Fig. 10** Antibacterial activity of each 3D scaffold using total plate count (TPC) method in (a)
405 Gram-positive cultures of *E. coli* and (b) Gram-negative cultures of *S. aureus* (n=3).

406 Moreover, the antibacterial activity of the scaffold against *E. coli* and *S. aureus* shows a
407 similar trend. The scaffold with the highest concentration of PFNR exhibits the fewest bacterial
408 colonies, indicating the most excellent antibacterial activity. Conversely, the scaffold with the
409 lowest concentration of PFNR showed the most minor antibacterial activity, demonstrating that
410 increasing the concentration of PFNR enhances antibacterial activity. Meanwhile, the
411 PCL_FNR_0.013 scaffold shows higher antibacterial activity than the PCL_PFNR_0.013 scaffold,
412 suggesting that non-coated FNR provides better antibacterial activity than PFNR and it can be
413 attributed to the hydrophobic surface of the material which can interact with the hydrophobic
414 membrane of the cell wall and rupture it [72].

415 **4. Conclusion**

We successfully fabricated a 3D-printed PCL scaffold reinforced with self-assembled FNR, achieving superior mechanical properties compared to other filler materials used in 3D-printed PCL scaffolds. We modified the surface of FNR with a P123 coating (PFNR) to introduce hydrophilic functional groups on the surface of FNR. By optimizing the concentration of PFNR, we effectively tuned the scaffold's hydrophilicity, leading to increased adhesion of biomolecules and enhanced cell proliferation. Additionally, both FNR and PFNR-reinforced scaffolds exhibited potent antibacterial activity against *S. aureus and E. coli*, addressing the critical challenge of preventing implant-associated infections. These findings highlight the potential of FNR and PFNR as advanced fillers in PCL-based scaffolds to provide tunable properties that enhance mechanical strength, biocompatibility, and antibacterial efficacy for bone tissue engineering.

References

1. F. Mahyudin, D. N. Utomo, H. Suroto, T. W. Martanto, M. Edward, and I. L. Gaol, Int. J. Biomater. **2017**, 7571523 (2017).
2. P. V. Giannoudis, Fracture Reduction and Fixation Techniques: Upper Extremities 1 (2018).
3. R. Wu, Y. Li, M. Shen, X. Yang, L. Zhang, X. Ke, G. Yang, C. Gao, Z. Gou, and S. Xu, Bioact. Mater. **6**, 1242 (2021).
4. M. Laubach, S. Suresh, B. Herath, M.-L. Wille, H. Delbrück, H. Alabdulrahman, D. W. Hutmacher, and F. Hildebrand, J. Orthop. Translat. **34**, 73 (2022).
5. D. Saul, M. M. Menger, S. Ehnert, A. K. Nüssler, T. Histing, and M. W. Laschke, Bioengineering **10**, 85 (2023).
6. W. B. Swanson, Z. Zhang, K. Xiu, T. Gong, M. Eberle, Z. Wang, and P. X. Ma, Acta Biomater. **118**, 215 (2020).
7. A. Wiese and H. C. Pape, Orthop. Clin. N. Am. **41**, 1 (2010).
8. D. N. Utomo, K. D. Hernugrahanto, M. Edward, L. Widhiyanto, and F. Mahyudin, Int. J. Surg. Case Rep. **58**, 178 (2019).
9. L. Hughes and C. P. Charalambous, *Engineering Advances in Promoting Tendon to Bone Healing* (Elsevier Inc., 2020).
10. L. Han, Z. Huang, Y. Zhu, and H. Li, Ceram. Int. **49**, 12895 (2023).
11. Z. Y. Qiu, Y. Cui, and X. M. Wang, *Natural Bone Tissue and Its Biomimetic* (Elsevier Ltd, 2019).
12. S. N. Angili, M. R. Morovvati, M. Kardan-Halvaei, S. Saber-Samandari, K. Razmjooee, A. M. Abed, D. Toghraie, and A. Khandan, Int. J. Biol. Macromol. **224**, 1152 (2023).
13. P. Han, G. A. Gomez, G. N. Duda, S. Ivanovski, and P. S. P. Poh, Acta Biomater. **163**, 259 (2023).
14. C. Garcia, Y. Orozco, A. Betancur, A. I. Moreno, K. Fuentes, A. Lopera, O. Suarez, T. Lobo, A. Ossa, A. Peláez-Vargas, and C. Paucar, Heliyon **9**, (2023).
15. A. Wibowo, C. Vyas, G. Cooper, F. Qulub, R. Suratman, A. I. Mahyuddin, T. Dirgantara, and P. Bartolo, Materials **13**, 512 (2020).

16. H. N. Chia and B. M. Wu, J. Biol. Eng. **9**, 1 (2015).
17. A. Seyedsalehi, L. Daneshmandi, M. Barajaa, J. Riordan, and C. T. Laurencin, Sci. Rep. **10**, 22210 (2020).
18. D. Liu, W. Nie, D. Li, W. Wang, L. Zheng, J. Zhang, J. Zhang, C. Peng, X. Mo, and C. He, Chem. Eng. J. **362**, 269 (2019).
19. S. H. Teoh, B. T. Goh, and J. Lim, Tissue Eng. Part A **25**, 931 (2019).
20. C. K. Arakawa and C. A. DeForest, in *Biology and Engineering of Stem Cell Niches* (Elsevier Inc., 2017), pp. 295–314.
21. W. Wang, J. R. P. Junior, P. R. L. Nalesso, D. Musson, J. Cornish, F. Mendonça, G. F. Caetano, and P. Bártolo, Mater. Sci. Eng. C **100**, 759 (2019).
22. W. Wang, G. Caetano, W. S. Ambler, J. J. Blaker, M. A. Frade, P. Mandal, C. Diver, and P. Bártolo, Materials **9**, 992 (2016).
23. G. Lo Re, S. Spinella, A. Boujemaoui, F. Vilaseca, P. T. Larsson, F. Adås, and L. A. Berglund, ACS Sustain. Chem. Eng. **6**, 6753 (2018).
24. R. Arambula-Maldonado and K. Mequanint, Mater. Adv. **3**, 5186 (2022).
25. R. Izadi, E. Ghavanloo, and A. Nayebi, Physica B Condens. Matter **574**, 311636 (2019).
26. W. Hong, X. Guo, T. Zhang, X. Zhu, Z. Su, Y. Meng, Y. Zhao, D. Xu, J. Pan, Y. Huang, H. Wang, K. Xu, H. Dong, C. Zhang, Y. Li, X. Yan, and X. Huang, Compos Part A Appl Sci Manuf **179**, 108043 (2024).
27. V. Dananjaya, S. Marimuthu, R. (Chunhui) Yang, A. N. Grace, and C. Abeykoon, Prog. Mater. Sci. **144**, 315 (2024).
28. S. Dastjerdi and B. Akgöz, Int. J. Eng. Sci. **142**, 125 (2019).
29. V. V. Zuev, Macromol. Symp. **301**, 157 (2011).
30. M. Rajagopalan, I. K. Oh, J. Palanivel, S. Sabarathinam, and J. Cifuentes-Faura, Sens. Actuators A Phys. **339**, 113510 (2022).
31. L. B. Sukhodub, L. F. Sukhodub, M. O. Kumeda, S. V. Prylutska, V. Deineka, Y. I. Prylutskyy, and U. Ritter, Carbohydr. Polym. **223**, 115067 (2019).
32. T. Sun, J. Huang, W. Zhang, X. Zheng, H. Wang, J. Liu, H. Leng, W. Yuan, and C. Song, Bioact. Mater. **21**, 44 (2023).
33. B. Nie, S. Huo, X. Qu, J. Guo, X. Liu, Q. Hong, Y. Wang, J. Yang, and B. Yue, Bioact. Mater. **16**, 134 (2022).
34. A. K. Thabit, D. F. Fatani, M. S. Bamakhrama, O. A. Barnawi, L. O. Basudan, and S. F. Alhejaili, Int. J. Infect. Dis. **81**, 128 (2019).
35. Y. Zhang, Z. Li, H. Guo, Q. Wang, B. Guo, X. Jiang, Y. Liu, S. Cui, Z. Wu, M. Yu, L. Zhu, L. Chen, N. Du, D. Luo, Y. Lin, P. Di, and Y. Liu, Adv. Sci. **11**, 2310292 (2024).
36. H. Setia Budi, M. Javed Ansari, S. Abdalkareem Jasim, W. K. Abdelbasset, D. Bokov, Y. F. Mustafa, M. A. A. Najm, and M. Kazemnejadi, Inorg. Chem. Commun. **139**, 109336 (2022).
37. L. K. Shrestha, Q. Ji, T. Mori, K. Miyazawa, Y. Yamauchi, J. P. Hill, and K. Ariga, in *Chem Asian J* (2013), pp. 1662–1679.
38. H. Amani, H. Arzaghi, M. Bayandori, A. S. Dezfuli, H. Pazoki-Toroudi, A. Shafiee, and L. Moradi, Adv. Mater. Interfaces **6**, 1900572 (2019).
39. C. W. Wong, K. C. Tsai, L. K. Shrestha, K. Ariga, and S. H. Hsu, Nanoscale **14**, 11152 (2022).
40. G. M. Z. F. Damke, E. Damke, P. de Souza Bonfim-Mendonça, B. A. Ratti, L. E. de Freitas Meirelles, V. R. S. da Silva, R. S. Gonçalves, G. B. César, S. de Oliveira Silva, W. Caetano, N. Hioka, R. P. Souza, and M. E. L. Consolaro, Life Sci. **255**, 117858 (2020).
41. J. Yu, H. Qiu, S. Yin, H. Wang, and Y. Li, Molecules **26**, 3610 (2021).
42. Q. Tang, S. Maji, B. Jiang, J. Sun, W. Zhao, J. P. Hill, K. Ariga, H. Fuchs, Q. Ji, and L. K. Shrestha, ACS Nano **13**, 14005 (2019).
43. M. Brązert, W. Kranc, P. Celichowski, M. Jankowski, H. Piotrowska-Kempisty, L. Pawelczyk, M. Bruska, M. Zabel, M. Nowicki, and B. Kempisty, Mol. Med. Rep. **21**, 1749 (2020).
44. M. Mira, A. Wibowo, G. U. N. Tajalla, G. Cooper, P. J. D. S. Bartolo, and A. Barlian, Mater. Adv. **4**, 6407 (2023).

45. Z. Chen, T. Zhou, H. Luo, Z. Wang, Q. Wang, R. Shi, Z. Li, R. Pang, and H. Tan, J. Nanobiotechnology **22**, 177 (2024).
46. A. Wibowo, G. U. N. Tajalla, M. A. Marsudi, G. Cooper, L. A. T. W. Asri, F. Liu, H. Ardy, and P. J. D. S. Bartolo, Molecules **26**, 1 (2021).
47. G. Wypych, in *Handbook of Fillers* (Elsevier, 2016), pp. 293–301.
48. N. G. Fischer and C. Aparicio, *On the Proliferation of Cell Proliferation Tests* (LTD, 2020).
49. S. M. J. Hashemi, S. E. Enderami, A. Barzegar, and R. N. Mansour, Tissue Cell **87**, 102318 (2024).
50. A. Rasyid, M. Y. Putra, and Yasman, Kuwait J. Sci. **50**, 615 (2023).
51. L. K. Shrestha, Q. Ji, T. Mori, K. Miyazawa, Y. Yamauchi, J. P. Hill, and K. Ariga, Chem. Asian J. **8**, 1662 (2013).
52. H. X. Ji, J. S. Hu, Q. X. Tang, W. G. Song, C. R. Wang, W. P. Hu, L. J. Wan, and S. T. Lee, J. Phys. Chem. C **111**, 10498 (2007).
53. H. M. Song and J. I. Zink, RSC Adv **9**, 4380 (2019).
54. J. I. Rosales-leal, M. A. Rodríguez-valverde, G. Mazzaglia, and P. J. Ramón-torregrosa, Colloids Surf. A: Physicochem. Eng. Asp. **365**, 222 (2010).
55. L. Dong, S.-J. Wang, X.-R. Zhao, Y.-F. Zhu, and J.-K. Yu, Sci. Rep. **7**, 13412 (2017).
56. R. Oftadeh, M. Perez-Viloria, J. C. Villa-Camacho, A. Vaziri, and A. Nazarian, J. Biomech. Eng. **137**, 010802 (2015).
57. B. Huang, C. Vyas, I. Roberts, Q. A. Poutrel, W. H. Chiang, J. J. Blaker, Z. Huang, and P. Bártolo, Mater. Sci. Eng. C **98**, 266 (2019).
58. L. Wang, Q. Chen, P. K. D. V. Yarlagadda, F. Zhu, Q. Li, and Z. Li, Mater. Des. **209**, 109986 (2021).
59. W. D. Callister and D. G. Rethwisch, *Fundamentals of Materials Science and Engineering: SI Version* (John Wiley & Sons, 2022).
60. C. S. D. Cabral, S. P. Miguel, D. de Melo-Diogo, R. O. Louro, and I. J. Correia, Carbon N Y **146**, 513 (2019).
61. F. Y. Hsieh, L. K. Shrestha, K. Ariga, and S. H. Hsu, Chem. Commun. **53**, 11024 (2017).
62. R. Desai, J. Cordeiro, B. Bastakoti, and K. Dellinger, Biomed. Sci. Instrum. **58**, (2022).
63. M. M. Mirhosseini, V. Haddadi-Asl, and S. S. Zargarian, J. Appl. Polym. Sci. **133**, (2016).
64. D. Wang and Q. Liu, Miner Eng **166**, 108443 (2021).
65. N. Slepickova Kasalkova, P. Slepicka, Z. Kolska, and V. Svorcik, in *Wetting and Wettability* (InTech, 2015).
66. Y. Bai, X. Wu, P. Ouyang, M. Shi, Q. Li, T. Maimaiti, S. Lan, S. T. Yang, and X. L. Chang, Environ. Sci. Nano **8**, 76 (2021).
67. N. S. Gsponer, E. Baigorria, E. N. Durantini, and M. E. Milanesio, Eur. Polym. J. **204**, 112678 (2024).
68. N. Y. Strutynska, I. I. Grynyuk, O. M. Vasyliuk, S. V. Prylutska, L. L. Vovchenko, I. A. Kraievska, N. S. Slobodyanik, U. Ritter, and Y. I. Prylutskyy, Arab. J. Sci. Eng. **47**, 7093 (2022).
69. J. D. Fortner, D. Y. Lyon, C. M. Sayes, A. M. Boyd, J. C. Falkner, E. M. Hotze, L. B. Alemany, Y. J. Tao, W. Guo, K. D. Ausman, V. L. Colvin, and J. B. Hughes, Environ. Sci. Technol. **39**, 4307 (2005).
70. M. Azizi-Lalabadi, H. Hashemi, J. Feng, and S. M. Jafari, Adv. Colloid Interface Sci. **284**, 102250 (2020).
71. M. Maas, Materials **9**, 617 (2016).
72. A. Kumar, G. Patel, and S. K. Menon, Chem. Biol. Drug Des. **73**, 553 (2009).

Conflict of Interest

We would like to declare that this work is original, has never been published and there is no conflict of interest.